



Spatial distribution, strength, and dealumination behavior of acid sites in nanocrystalline MFI zeolites and their catalytic consequences

Kyoungsoo Kim^a, Ryong Ryoo^a, Hee-Dong Jang^b, Minkee Choi^{c,*}

^a Department of Chemistry, and Graduate School of Nanoscience and Technology (WCU), Korea Advanced Institute of Science and Technology, Daejeon 305-701, Republic of Korea

^b Department of Industrial Materials Research, Korea Institute of Geoscience and Mineral Resources, Yuseong-gu, Daejeon 305-350, Republic of Korea

^c Department of Chemical and Biomolecular Engineering, Korea Advanced Institute of Science and Technology, Daejeon 305-701, Republic of Korea

ARTICLE INFO

Article history:

Received 7 November 2011

Revised 12 January 2012

Accepted 13 January 2012

Available online 15 February 2012

Keywords:

Nanocrystalline zeolite

Hierarchical zeolite

Acidity

Dealumination

Hydrothermal stability

Steaming

MTG

Cracking

ABSTRACT

The distribution, acid strength, and steam stability of internal and external acid sites were systematically investigated for nanocrystalline MFI zeolites with different crystallite size (2–300 nm), which were obtained using gemini-surfactants having different alkyl chain lengths. FT-IR spectroscopy using pyridine and 2,6-di-tert-butylpyridine as a base probe revealed that the concentration of external acid sites increased with a decreasing crystallite size. The external sites were weaker than the internal sites in acid strength, but could still catalyze *n*-octane cracking reactions that require the strongest acid strength among various acid-catalyzed reactions. Most notably, the external acid sites of zeolites exhibited remarkably higher steam stability at 873 K than the internal acid sites. Such an observation was supported by the catalytic results in methanol to dimethylether (DME) and gasoline conversion, and the Claisen–Schmidt condensation involving bulky molecules.

© 2012 Elsevier Inc. All rights reserved.

1. Introduction

Zeolites, crystalline microporous aluminosilicates, have played a crucial role as a heterogeneous acid catalyst in the petrochemical industry and fine chemical syntheses. Their remarkable successes in industrial applications can be attributed to strong framework acidity and molecular sieving ability due to the presence of uniform micropores of molecular dimension [1–3]. Although the micropores in zeolites enabled shape-/size-selective catalytic processes, the sole presence of micropores in micrometer-sized zeolite crystals can significantly limit the molecular diffusion and decrease the effectiveness factor of a zeolite catalyst [4–7]. The slow diffusion in zeolite crystals can also lead to low catalytic selectivity and durability due to coke formation [4–7].

To overcome the diffusion limitations, scientific efforts have been devoted to developing new zeolite-type molecular sieves having extra-large micropores (>1.5 nm). Some of the extra-large micropore systems have been reported, but most of them were constructed with non-aluminosilicate frameworks such as silico-germanates [8] and metalophosphates [9,10]. The physicochemical properties of these materials, such as acidity and hydrothermal

stabilities, have not yet been fully elucidated. After the discovery of MCM-41-type ordered mesoporous materials in 1992, MCM-41-type aluminosilicates with mesopores (2–50 nm in diameter) were also extensively studied as a solid acid catalyst [3,11–13]. The materials, generally synthesized using the self-assembly of an organic surfactant as a mesopore template, possess a high surface area (up to 1200 m² g⁻¹) and ordered mesoporous structures. Due to the amorphous feature of the pore walls, however, these materials showed much lower hydrothermal stability and acidity than the crystalline zeolites [3,10,14].

Another strategy for enhancing diffusion in zeolites is to decrease the diffusion path length within the microporous crystals by reducing the crystal (or framework) thickness [4–7]. The strategy provides the advantages of using the strong acidity and shape selectivity of well-known zeolite structures, in addition to enhanced molecular diffusion. Zeolites with a reduced framework thickness can be obtained by crystallizing zeolites into nanocrystal morphology [15] or hierarchical structures possessing secondary mesoporosity within microporous zeolite crystals. Such materials have been synthesized by careful optimization of crystallization conditions [15], selective framework etching (dealumination and desilication) of pre-synthesized zeolites [16,17], zeolite synthesis in a confined space of solid templates [6,18], and addition of organosilanes into the synthesis compositions [19,20]. Very

* Corresponding author.

E-mail address: mkchoi@kaist.ac.kr (M. Choi).

recently, Ryoo et al. reported that the surfactants with zeolite structure-directing groups can direct ultrathin zeolite structures possessing large mesoporosity [21,22].

Due to the reduced diffusion path length, such zeolites exhibited significantly enhanced molecular diffusion over bulk zeolite crystals [23–25]. The fast molecular diffusion leads to enhanced activity and selectivity in benzene ethylation [24,26] and hydrocarbon isomerization reactions [27,28]. Acid sites located at the external surface (or mesopore wall) of the hierarchical zeolites could catalyze reactions involving bulky molecules that cannot enter the zeolite micropores [29]. Notably, the zeolite catalyst exhibited significantly slower deactivation. The enhanced catalyst durability was attributed to the fast diffusion of coke precursors out of zeolite micropores [21,30,31].

Despite the extensive studies on the nanocrystalline or micro-/mesoporous hierarchical zeolites, most of the research has focused on material synthesis and pore structural analysis. So far, little information on the acidity and hydrothermal stability of these zeolites has been known [32–35], although they are the ultimate factors determining the catalytic applicability of these materials. Since the conventional zeolites possess very low external surface area, the catalytic contributions of the external acid sites are not generally very significant. In contrast, the nanocrystalline zeolites are expected to contain a considerable amount of external acid sites due to the enlarged external surface area. This can lead to the remarkably different catalytic behaviors of the nanocrystalline zeolites as compared to the conventional zeolites. In addition, many solid acid catalysts including even crystalline zeolites suffered from structural damage or loss of active sites due to their limited hydrothermal stability during catalyst regeneration in acid-catalyzed reactions (e.g., FCC reaction) [3]. The hydrothermal stability of zeolites is also of prime importance in designing environmental catalysts for vehicular applications [36,37]. In this respect, a comprehensive study to elucidate the spatial distribution, acid strength, and hydrothermal stabilities of aluminum sites in the nanocrystalline zeolites is highly important.

In the present work, MFI zeolites (Si/Al \sim 30) with three different crystallite size and shape were synthesized using gemini-type quaternary ammonium surfactants as a structure-directing agent (SDA) (Scheme 1). These surfactant molecules, easily and economically synthesizable in a laboratory, can direct a MFI zeolite structure having different crystallite sizes without the use of an additional molecular template such as tetrapropylammonium. By simply changing the alkyl chain length of the surfactants, MFI zeolites with a wide range of BET surface areas (360–540 m² g⁻¹) could be prepared (conventional MFI: \sim 350 m² g⁻¹). FT-IR spectroscopy using pyridine (Py) and 2,6-di-tert-butylpyridine (2,6-DTBP) as a base probe was used to analyze the relative amount, acid strength, and hydrothermal stabilities of internal and external acid sites in these zeolites. We correlated such structural information to the catalytic consequences in methanol to dimethylether (DME) and gasoline conversion, the Claisen–Schmidt condensation reaction involving bulky molecules, and *n*-octane cracking. In particular, we presented extra-high durability of nanocrystalline zeolites against high-temperature steam due to the outstanding hydrothermal stability of external acid sites. To the best of our knowledge, such extraordinary steam stability of external acid sites has not been reported so

far, probably due to the negligible concentration of these sites in conventional zeolites.

2. Experimental

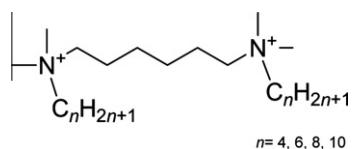
2.1. Sample preparation

Gemini-type quaternary ammonium surfactants with a formula of C_{*n*}H_{2*n*+1}-N⁺(CH₃)₂-C₆H₁₂-N⁺(CH₃)₂-C_{*n*}H_{2*n*+1} (simply designated by C_{*n*}-6-*n*, *n* = 4, 6, 8, 10) were synthesized via a one-step reaction between tetramethyl diaminoethane and corresponding bromoalkanes. In a typical synthesis of C₁₀-6-10, 26.5 g (0.12 mol) 1-bromodecane (TCI) and 11.6 g (0.06 mol) N,N,N',N'-tetramethyl-1,6-diaminohexane (Aldrich) were dissolved in 80 ml of acetonitrile and reacted under magnetic stirring at 333 K for 6 h. After cooling to room temperature, the precipitated product was filtered, washed with cold diethyl ether, and dried in a vacuum oven at 323 K for the removal of organic solvent. The products were identified by ¹HNMR in a CDCl₃ solution using a Bruker Avance instrument (300 MHz).

Zeolites and mesoporous aluminosilicate were hydrothermally synthesized using the gemini-surfactants as an SDA. The starting molar composition was 1.25 Al₂O₃: 30 Na₂O: 100 SiO₂: 10 SDA: 24 H₂SO₄: 4000 H₂O. Water glass (an aqueous solution of sodium silicate, Si/Na = 1.75, 29 wt.% SiO₂) and aluminum sulfate octadecahydrate (98%, Aldrich) were used as a silica and an aluminum source, respectively. After continuous stirring for 1 h at 333 K, the resultant gel was transferred into a Teflon-lined stainless-steel autoclave. This autoclave was hydrothermally heated at 403 K for 6 d under tumbling (60 rpm). The resultant products were filtered, thoroughly washed with deionized water, and dried at 393 K. All the samples were calcined at 823 K for 4 h in dry air to remove the SDA. To make an H⁺-form, the calcined materials were ion-exchanged with NH₄⁺ three times using 1 M NH₄NO₃ aqueous solution, followed by calcination at 823 K. The resultant materials were denoted as AS-*n*, where *n* indicated the alkyl chain length in C_{*n*}-6-*n* SDA. To check the hydrothermal stability of the materials, 1 g AS-*n* samples were placed in a vertical quartz reactor equipped with a fritted disk (30 mm in diameter) and treated with steam (10% in N₂, 60 ml min⁻¹) at 873 K for 2 h. The resultant samples were denoted as ST-*n*. To check the hydrothermal stability under more harsh steam condition, 1 g AS-4 and AS-8 samples were also treated with 100% steam at 973 K for 2 h.

2.2. Characterization

Si/Al ratios were determined by inductively coupled plasma atomic emission spectroscopy (ICP-AES) using an OPTIMA 4300 DV instrument (Perkin Elmer). Powder X-ray diffraction (XRD) patterns were recorded using a Rigaku Multiflex diffractometer equipped with CuK_α radiation (40 kV, 30 mA). Organic contents in as-synthesized samples were measured by thermogravimetric analysis using a TGA Q500 (Thermal Analysis Instruments Inc.). The temperature was increased to 1073 K under flowing air (60 ml min⁻¹) at a constant ramping rate of 20 K min⁻¹. N₂ adsorption/desorption isotherms were measured with Micromeritics TriStar II adsorption volumetric analyzer at the liquid N₂ temperature (77 K). Prior to the adsorption measurements, all samples were degassed in a vacuum for 3 h at 573 K. The specific surface area was determined from the adsorption branch in a *P/P*₀ range between 0.05 and 0.20, using the Brunauer–Emmett–Teller (BET) equation. The external surface areas of the zeolites were determined by measuring BET surface areas of as-synthesized zeolite samples without SDA removal. The as-synthesized samples were degassed at 423 K for 5 h before the adsorption experiments. SDA contents determined by thermogravimetric analysis were used to correct the



Scheme 1. Molecular structure of gemini-surfactants used as an SDA for zeolite synthesis.

weight of zeolite samples. The pore size distributions were determined using non-local density functional theory (DLT). The micropore volumes were determined by *t*-plot method, and total pore volumes were estimated at $P/P_0 = 0.95$. Scanning electron micrographs (SEMs) were taken with a Magellan400 (FEI) at a low landing energy (1 kV) without crushing or metal coating. Transmission electron micrographs (TEMs) were collected by Tecnai G2 F30 (FEI) at 300 kV acceleration voltage after mounting the samples on a carbon grid (300 mesh) using ethanol dispersion.

For FT-IR measurement, all the samples were pressed into a self-supporting wafer (8–12 mg cm⁻²) [38]. Before the IR measurements, each sample was degassed at 773 K for 2 h in a vacuum and cooled to room temperature in an IR cell. For the measurement of total and external acidity, pyridine (Py) and 2,6-di-*tert*-butylpyridine (2,6-DTBP) were used as a base probe molecule, respectively. Py and 2,6-DTBP were adsorbed on the degassed sample wafer for 1 h at room temperature and 423 K, respectively. The weakly bound species were desorbed for 1 h in a vacuum at 423 K. After cooling to room temperature, IR spectra were collected using an FT-IR spectrometer (Bruker Vector 33) with 40 scans and 2 cm⁻¹ resolution in the 4000–400 cm⁻¹ range. To distinguish strong acid sites, IR spectra were also collected after desorption of Py molecules at 573 K instead of 423 K. To directly compare the band area of all samples, all spectra were normalized using the overtone and combination vibrations between 2080 and 1750 cm⁻¹. For quantification of total Brønsted acid sites, molar extinction coefficient ($\epsilon = 5.98 \text{ cm}^2 \text{ mmol}^{-1}$) of Py IR band at $\nu = 1545 \text{ cm}^{-1}$ was used. This value was determined for a reference material (H-ZSM-5, Si/Al = 40 from Zeolyst International; 0.41 mmol acid sites g⁻¹). For calculating the concentration of external acid sites, molar extinction coefficient ($\epsilon = 10.10 \text{ cm}^2 \text{ mmol}^{-1}$) of 2,6-DTBP IR band at $\nu = 1616 \text{ cm}^{-1}$ was determined by assuming that concentration of the external Brønsted acid sites in AS-10 is equal to concentration of the total Brønsted acid sites. This assumption is reasonable since AS-10 sample contains solely mesoporous structure.

2.3. Catalytic reaction measurement

Methanol to dimethylether (DME) conversion reaction was carried out at 473 K in a Pyrex plug-flow reactor (inner diameter = 13 mm) using 0.05 g of zeolite as a catalyst. The reaction temperature was measured by a K-type thermocouple inserted in the reactor through a thermocouple well. Before the reaction, the catalyst was activated at 823 K for 2 h in an air flow (30 ml min⁻¹). For the reaction, methanol vapor was injected into the catalyst bed using a syringe pump in a N₂ flow (WHSV = 9.5 g g⁻¹ h⁻¹, 50 ml min⁻¹ flow rate). The reactor effluent was analyzed by an online gas chromatography (GC, Younglin, Acme-6000) equipped with a flame ionization detector and a capillary column (HP-Plot-Q, J&W).

MTG (Methanol-to-gasoline) reaction was similarly carried out at 623 K except the use of different space velocity (WHSV = 19 g g⁻¹ h⁻¹, 50.5 ml min⁻¹ flow rate). The reactor effluent was analyzed by an online gas chromatography (GC, Younglin, Acme-6000) equipped with a flame ionization detector and a capillary column (GasPro, J&W). The reaction conversion was calculated by considering oxygen-free hydrocarbon species as a product and oxygenates (*i.e.*, methanol and dimethylether) as an unconverted species.

A flavanone synthesis reaction was carried out in a N₂ atmosphere using a Pyrex batch reactor (EYELA chemistation) equipped with a reflux condenser [29]. A reaction mixture containing benzaldehyde (0.75 g, 7 mmol), 2-hydroxyacetophenone (0.476 g, 3.5 mmol), and 0.05 g of catalyst was heated with stirring for 6 h at 423 K. After the reaction, the mixture was cooled and diluted

with 3 ml of dichloromethane. The diluted samples were analyzed by a GC (α -dex 120 column, Supelco).

n-octane cracking reaction was carried out at 773 K in the Pyrex plug-flow reactor using 0.05 g of zeolite as a catalyst. Before the reaction, the catalyst was activated at 823 K for 2 h under an air flow (30 ml min⁻¹). For the reaction, *n*-octane vapor was injected into the catalyst bed using a syringe pump under N₂ flow (WHSV = 140 g g⁻¹ h⁻¹, 50.5 ml min⁻¹ flow rate). The reactor effluent was analyzed by the online GC equipped with the flame ionization detector and a capillary column (Petrocol™ DH, Supelco).

3. Results and discussion

3.1. Structural properties of the zeolites templated by gemini-surfactants

XRD patterns for the aluminosilicate samples synthesized using the gemini-surfactants as an SDA are shown in Fig. 1a. Up to the alkyl chain length (*n*) of 8, the resultant aluminosilicate materials (AS-4, 6 and 8) exhibited a typical XRD pattern for an MFI structure. This result is consistent with previous results showing that the linear alkylammonium polycations can act as an efficient SDA for an MFI zeolite structure [39]. The XRD patterns gradually broadened with an increasing alkyl chain length of the gemini-surfactant, which indicated a decreasing crystallite size of the zeolite.

At alkyl chains longer than 8, MCM-41-type mesoporous aluminosilicates with amorphous framework formed. For instance, the AS-10 sample did not exhibit well-resolved wide angle XRD peaks but only showed a broad XRD peak at $15^\circ < 2\theta < 30^\circ$. The sample showed a well-resolved peak at $2\theta \sim 5^\circ$ due to the ordered arrangement of mesopores. The presence of single peak at low-angle regime indicates that the material possess only a short-range mesostructural order similar to KIT-1 [40] having wormhole-like disordered mesopores. The formation of mesoporous aluminosilicate with a long-chain surfactant indicates that the surfactants can be self-assembled into a micelle at the synthesis temperature (403 K) via hydrophobic interactions between long-chain alkyl groups. Such micelle acts as a supramolecular template to direct the formation of a mesoporous structure. Elemental analysis of the as-synthesized samples shows that N/Si molar ratios for AS-4, 6, and 8 samples are around 0.06, while AS-10 sample possesses significantly higher ratio of 0.14. Beck et al. reported similar N/Si molar ratios for the materials that were synthesized via the molecular and the supramolecular templating actions of single-chain alkylammonium surfactants [41].

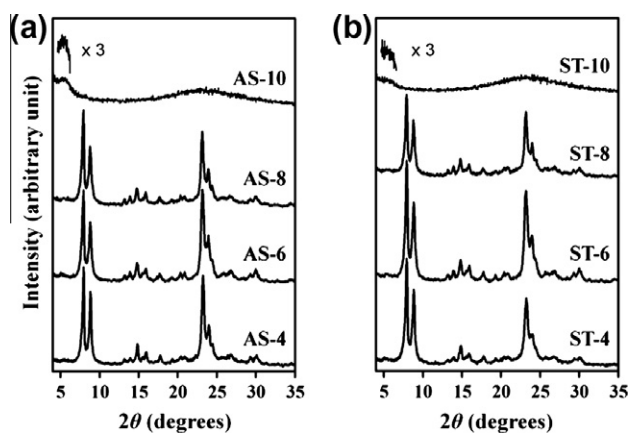


Fig. 1. XRD patterns for the aluminosilicate samples obtained using gemini-type surfactants with different alkyl chain length (a) before and (b) after the steam treatment at 873 K for 2 h.

SEM and TEM images for the aluminosilicate samples are given in Fig. 2. SEM investigation revealed that the AS-4 sample possessed globular morphologies having a rough crystal surface. Although the crystal surface was rough in the SEM image, TEM investigations showed that the material had a large single-crystalline domain (>300 nm). Existence of secondary meso- or macroporosity was not observed within the crystals. The AS-6 sample exhibited a sponge-like morphology in the SEM image, which was composed of a nanosized zeolite framework. The TEM images revealed that the material was composed of 10–20 nm zeolite crystallites that are 3-dimensionally interconnected to form a sponge-like morphology including a large intercrystalline void volume. The AS-8 sample was built with the random assembly of thin 'flake-like' zeolite crystals as indicated by the SEM image. TEM investigation showed that the flake-like morphology resulted from the zeolite crystals that were anisotropically grown to form a 2-dimensional sheet-like structure with 2–6 nm thickness.

Electron micrographs of the AS-10 sample showed that the material possessed irregular morphologies including disordered mesoporous structure. No framework crystallinity was indicated by TEM investigation, which is also consistent with the previous XRD data.

The electron microscopic observations for the zeolitic (crystalline) samples (AS-4, 6 and 8) were consistent with the XRD data showing that the zeolite crystal thickness decreases with an increasing alkyl chain length of gemini-surfactant molecule. In a general sense, the zeolites synthesized in the presence of organic SDA possess a smaller crystallite size than the zeolites synthesized without SDA. Such phenomena can be attributed to the stabilization of zeolite crystallites via the steric barrier created by an excess of SDA molecules adsorbed on the crystallite surface [42]. Such a steric barrier can hinder the fusion or ripening of small zeolite crystallites. Since the steric barrier increases with the volume of SDA [42], it is reasonable to expect that a longer alkyl chain length

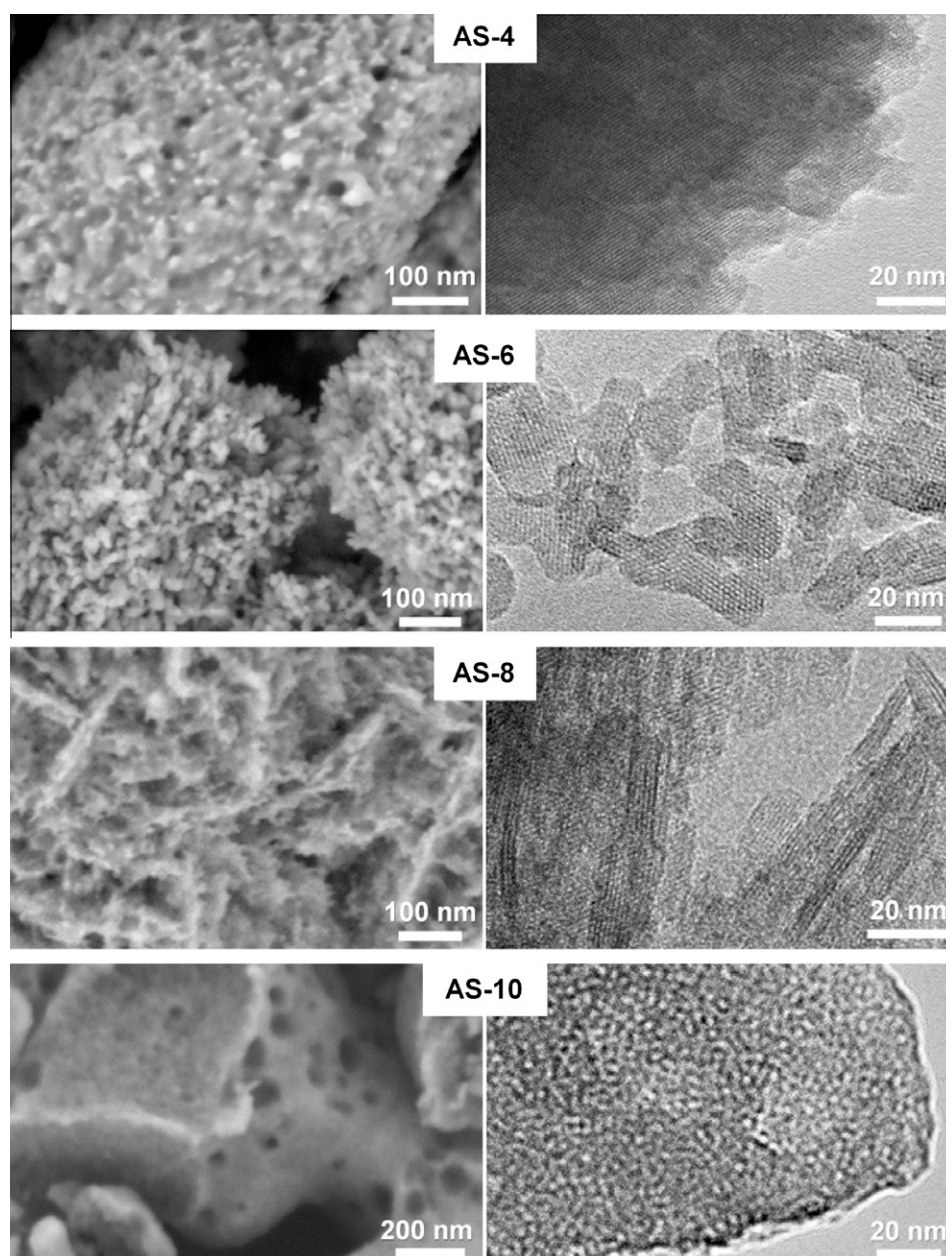


Fig. 2. Electron micrographs (left column: SEM, right column: TEM) of AS-4, AS-6, AS-8 and AS-10.

of the gemini-surfactant would provide more steric stabilization and hence produce smaller zeolite crystallites. For verifying the presence of external SDA molecules adsorbed on the crystallite surface, thermogravimetric analyses of the as-synthesized aluminosilicates were carried out before and after SDA extraction with HCl/ethanol solution. The organic SDA contents (decomposed in the range of 500–800 K) of as-synthesized AS-4, 6 and 8 were 9.7 wt.%, 11.0 wt.% and 14.9 wt.%, respectively. After the HCl/ethanol extraction, the organic contents were decreased to 8.8 wt.%, 9.8 wt.% and 9.7 wt.%, respectively. The decreased organic content after the extraction indicates that considerable amount of organic SDA are present on the zeolite external surfaces.

In the case of the AS-8 sample, special explanation would be necessary for the anisotropic crystal growth into 2-dimensional sheet-like zeolite crystallites. Such an anisotropic zeolite structure is quite similar to the ultrathin MFI zeolites that are obtained by asymmetric diquaternary ammonium surfactants having a long C22 alkyl chain (corresponding to C₂₂₋₆₋₆ in our notation) [21]. In that work, sheet-like zeolite crystals with a unit-cell thickness (2 nm) along the crystal *b*-axis were directed by diquaternary ammonium groups while the hydrophobic chains restricted the excessive growth of zeolites and induced self-assembly into the mesostructure. We believe that the present C₈₋₆₋₈ surfactant also directed the formation of sheet-like zeolite crystals in the same mechanism due to the similar head group structure. The absence of a long alkyl chain, however, occasionally allows the excessive growth of zeolite along the *b*-direction, and a crystal thickness larger than 2 nm could be achieved (2–6 nm).

The pore structural properties of the aluminosilicates material analyzed from N₂ adsorption/desorption isotherms (Fig. 3a) are summarized in Table 1. The AS-4 sample showed a typical type-I isotherm indicating a solely microporous structure. The absence of secondary meso- or macroporosity resulted in a small BET surface area (360 m² g⁻¹). The AS-6 sample exhibited secondary mesoporosity (10 < diameter < 40 nm) with a high surface area (480 m² g⁻¹). The mesopore size determined using the DFT method was centered at 20 nm (Fig. S1 in the Supplementary material), which is consistent with the size of the intercrystalline voids in the TEM images. The AS-8 sample exhibited the highest surface area (540 m² g⁻¹) due to the smallest crystallite size as confirmed by XRD and TEM analysis. Pore size distribution using the DFT method indicated that the material possessed very small mesopores centered at ~2 nm, which might be formed by the stacking of sheet-like zeolite structures. The type-H4 hysteresis loop in the adsorption/desorption isotherm, a general characteristic of narrow slit-like pores [43], indicated that the mesopores would

have a slit-like pore geometry. It is noteworthy that the material also possessed large macroporosity (>50 nm) that is clearly distinguished in SEM images (Fig. 2 and Fig. S1). The difference among the BET surface area of AS-4, 6 and 8 can be attributed to the difference of the external surface area of the samples. The external surface areas were determined by measuring BET surface areas of as-synthesized zeolite samples without SDA removal (Table 1). The result clearly shows that AS-6 (85 m² g⁻¹) and AS-8 (100 m² g⁻¹) samples possess much larger external surface area than AS-4 (25 m² g⁻¹). All the zeolitic materials (AS-4, 6 and 8) possessed similar micropore volume (~0.13 ml g⁻¹), which corresponded to the generally reported micropore volume of MFI zeolite. The AS-10 sample exhibited a sharp condensation step at a pressure range of 0.1–0.2, which corresponded to the uniform mesopore size distribution centered at 2.4 nm. The material showed negligible microporosity (~0 ml g⁻¹) similar to other MCM-41-type materials synthesized under basic medium [44].

3.2. Effects of steam treatment on the structural properties of the aluminosilicate materials

The hydrothermal stability of aluminosilicate materials is important for acid catalytic applications, since high-temperature steam is generated during the regeneration of catalysts in many acid catalytic reactions (e.g., FCC reaction) [3]. Under these conditions, the pore and crystalline structure could be damaged and lead to the diminished catalytic functions of the materials. Due to the very small crystallite size of the nanocrystalline zeolites, these materials could be more prone to structural change than bulk zeolite crystals. In this respect, we analyzed the framework and pore structure of the aluminosilicate samples after steam treatment at 873 K for 2 h. Hereafter, steam-treated samples will be denoted as ST-*n*.

XRD analysis (Fig. 1b) indicated that the zeolitic samples (ST-4, 6, and 8) still possessed highly crystalline structure as indicated by well-resolved peaks in the wide-angle regime. In the case of amorphous mesoporous aluminosilicate (ST-10), intensity for the XRD peak at $2\theta \sim 5^\circ$ decreased significantly. The result indicated that mesostructural order was significantly lost during the steam treatment. N₂ adsorption/desorption (Fig. 3b and Table 1) also confirmed that the pore structural properties of zeolitic samples were almost intact. The BET surface area and pore volume were diminished much more slightly compared with the amorphous material (ST-10). These results indicated that the crystalline zeolite frameworks can show remarkably higher hydrothermal stability than the amorphous framework, although they are composed of tiny nanocrystallites [35].

3.3. Distribution, strength, and dealumination behavior of acid sites

In addition to the pore structure, the spatial distribution, strength, and steam-dealumination behavior of acid sites are also decisive factors determining the catalytic functions of the aluminosilicate materials. In this respect, we analyzed the acidity of the materials by FT-IR before and after the steam treatment at 873 K. The total and external acidity of aluminosilicates were separately investigated after adsorbing pyridine (Py) and 2,6-di-*tert*-butylpyridine (2,6-DTBPY) followed by desorption of weakly bound species at 423 K. The 2,6-DTBPY is too bulky (0.8 nm) to enter the 10-membered channels (0.51–0.56 nm) of the MFI zeolite and hence can only be adsorbed on the acid sites at the zeolite external surface. In contrast, Py has a sufficiently small size (0.5 nm) and can titrate both the internal and the external acid sites.

The hydroxyl stretching vibration region of IR spectra before and after the adsorption of Py and 2,6-DTBPY is given in Fig. 4. All the zeolitic materials (AS-4, 6 and 8) exhibited bands at 3725 and 3610 cm⁻¹, which were attributed to the stretching vibrations

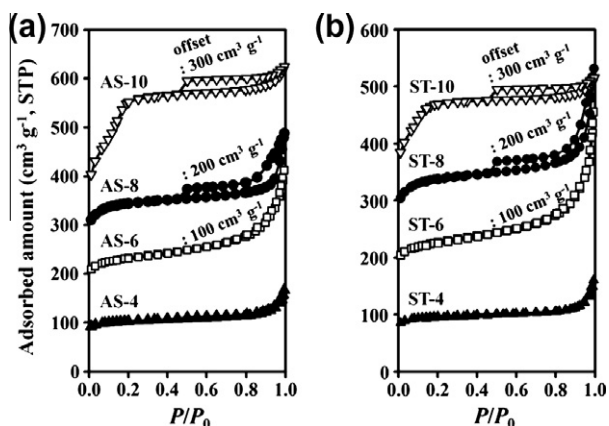


Fig. 3. N₂ adsorption/desorption isotherms at 77 K for (a) the pristine aluminosilicate materials and (b) the materials treated with steam (10%) at 873 K for 2 h.

Table 1
Structural properties of the aluminosilicate materials.

Sample	Si/Al ^a	S _{BET} ^b (m ² g ⁻¹)	S _{ext} ^c (m ² g ⁻¹)	V _{micro} ^d (ml g ⁻¹)	V _{total} ^e (ml g ⁻¹)
AS-4	30.3	360	25	0.13	0.22
ST-4	30.6	350	–	0.12	0.20
AS-6	31.6	480	85	0.13	0.40
ST-6	32.2	450	–	0.12	0.41
AS-8	31.8	540	100	0.13	0.41
ST-8	31.2	510	–	0.13	0.40
AS-10	32.9	960	320	~0	0.47
ST-10	33.9	660	–	~0	0.31

^a Si/Al ratio obtained by ICP-AES analysis.

^b BET surface areas calculated at $P/P_0 = 0.05$ – 0.2 .

^c The external surface areas determined by calculating BET surface areas of as-synthesized samples without SDA removal.

^d The micropore volumes determined by t -plot analysis.

^e The total pore volume evaluated at $P/P_0 = 0.95$.

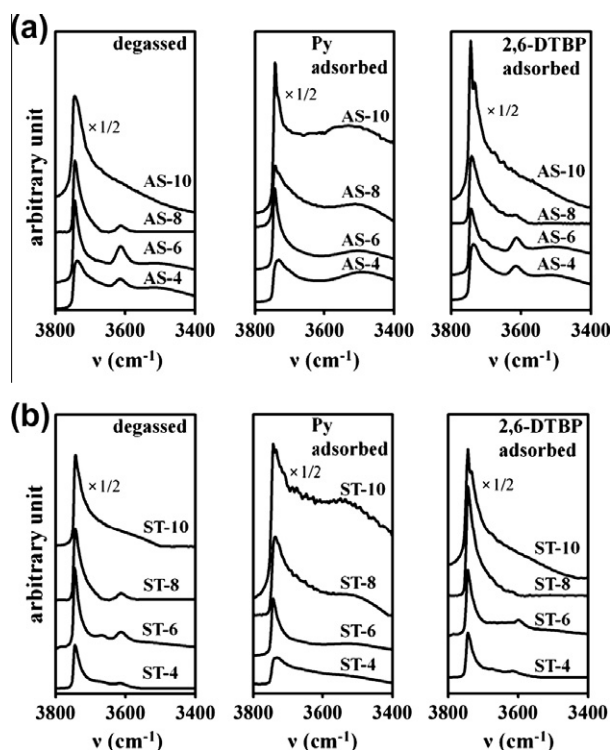


Fig. 4. IR spectra of degassed, pyridine (Py)-adsorbed, and 2,6-ditertbutyl pyridine (2,6-DTBP)-adsorbed aluminosilicates (a) before and (b) after the steam treatment at 873 K for 2 h under 10% steam.

of terminal silanol and bridging hydroxyl groups (*i.e.*, acidic hydroxyl group) in zeolite, respectively. Amorphous aluminosilicate (AS-10) exhibited very broad band at 3610 cm^{-1} and the band at 3725 cm^{-1} having significantly larger area than other samples. The result indicates that AS-10 sample with amorphous framework possesses heterogeneous distribution of acid sites and large amount of defect silanol groups. The band area at 3610 cm^{-1} increases in the order of $\text{AS-8} < \text{AS-4} < \text{AS-6}$, which corresponds to the order of total acid concentration (Fig. 4a). This band completely disappeared after Py adsorption, indicating that Py can titrate all the acid sites.

The adsorption of bulky 2,6-DTBP leads to almost complete disappearance of 3610 cm^{-1} band for AS-8 sample, which indicates that most of acidic hydroxyl groups are located at the external surface that are accessible to 2,6-DTBP. In comparison, AS-4 and AS-6 sample showed considerable band area at 3610 cm^{-1} . This result shows that AS-4 and AS-6 samples possess larger amount of internal acid sites than AS-8. After the steam treatment, the band area

of the acidic hydroxyl group (3610 cm^{-1}) for the degassed samples (Fig. 4b) was decreased, indicating the removal of acid sites due to steam dealumination. Notably, more significant decrease in the band area was observed for the samples with smaller external surface area. AS-8 sample exhibited no significant change in 3610 cm^{-1} band area, while AS-4 sample showed significant decrease. After the 2,6-DTBP adsorption, ST-4 and ST-6 samples showed significantly decreased band area at 3610 cm^{-1} , indicating that internal acidic hydroxyl groups were significantly damaged by steam treatment.

More quantitative determination of total and external Brønsted acid sites were carried out using the IR bands at 1545 cm^{-1} [45] and 1616 cm^{-1} [38,46] after adsorption of Py and 2,6-DTBP, respectively (Fig. 5). These IR bands are the characteristic bands for the probe molecules that interact with the Brønsted acid sites. In Fig. 6, the concentrations of total and external Brønsted acid sites are shown for the materials before and after the steam treatment. The concentrations of total Brønsted acid sites were in the range of 0.27 – 0.41 mmol g^{-1} for the pristine materials. After the 10% steam treatment at 873 K, the total acid concentration was decreased due to framework dealumination. Notably, the dealumination occurred more seriously as the crystallite size of the zeolites increased. AS-4 with submicron crystallite size exhibited 51.7% dealumination of total acid sites, while AS-8 with 2–6 nm crystallites showed only 9% dealumination. The AS-10 sample with amorphous framework showed almost negligible degree of dealumination (<3%). The concentration of external Brønsted acid sites increased with a decreasing crystallite size of zeolitic materials

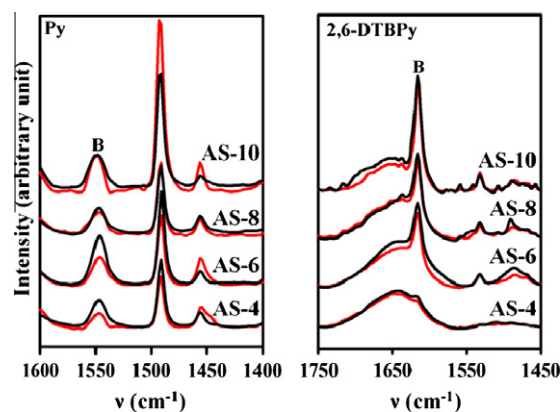


Fig. 5. IR spectra of pyridine (Py) and 2,6-ditertbutyl pyridine (2,6-DTBP) adsorbed on the pristine aluminosilicates (black line) and the steam-treated aluminosilicates (red line) after desorbing weakly bound species. 'B' peaks were integrated to quantify the Brønsted acidity of the samples. (For interpretation of the references to color in this figure legend, the reader is referred to the web version of this article.)

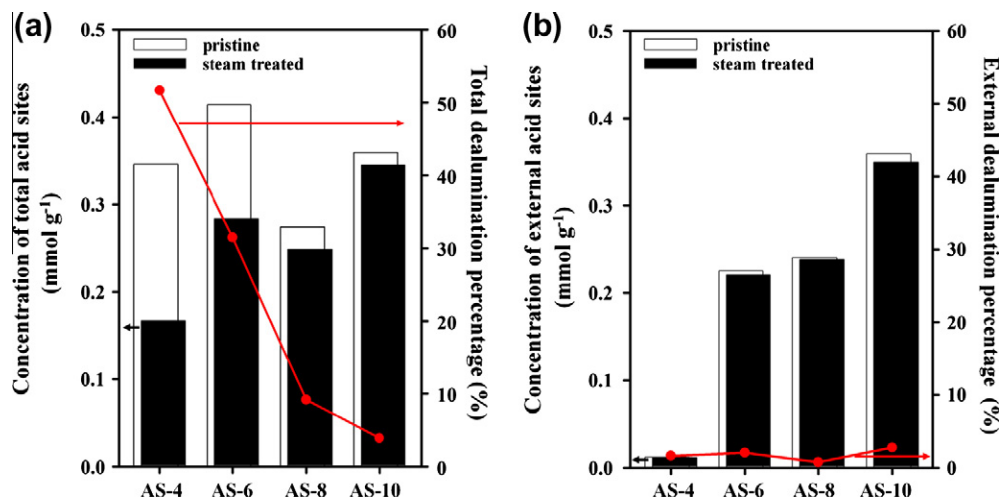


Fig. 6. Concentration of (a) total acid and (b) external acid sites before and after the steam treatment at 873 K for 2 h.

(Fig. 6b), which can be attributed to the increasing external surface area of the zeolite crystals. The AS-10 sample exhibited the highest adsorption of 2,6-DTBPY due to the open mesoporous structure. In contrast to the total acid sites, the concentrations of external acid sites did not significantly change for all the samples even after the steam treatment (<5%). The present result strongly supports that the external acid sites are remarkably more resistant to steam dealumination than the internal acid sites. However, we confirmed that both internal and external acid site were significantly dealuminated under much more severe steam conditions, such as 973 K under 100% steam for 2 h. Accordingly, AS-4 and AS-8 showed 90% and 88% loss of total acid sites (Fig. S2 in the Supplementary material).

The distribution of acid strength before and after the steam treatment was studied by comparing the IR peak area after desorption of adsorbed Py at 573 K instead of 423 K (Fig. S3 in the Supplementary material). Although the desorption of Py at elevated temperatures can be affected not only by strength of Brønsted acid sites but also by the kinetics of desorption/readsorption processes, the ratio of the IR peak area measured after Py desorption at 573 K and 423 K can qualitatively indicate the fraction of strong acid sites among the total acid sites (Fig. 7). The results in Fig. 7 showed that the zeolitic materials with larger crystallites had more strong acid

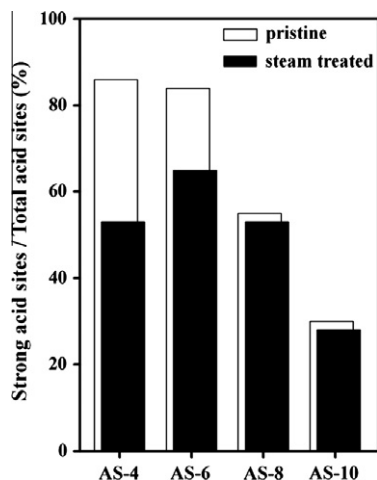


Fig. 7. Fraction of strong acid sites among total acid sites for the aluminosilicate materials. The fraction was calculated from the ratio of the IR peak area measured after Py desorption at 573 K and 423 K.

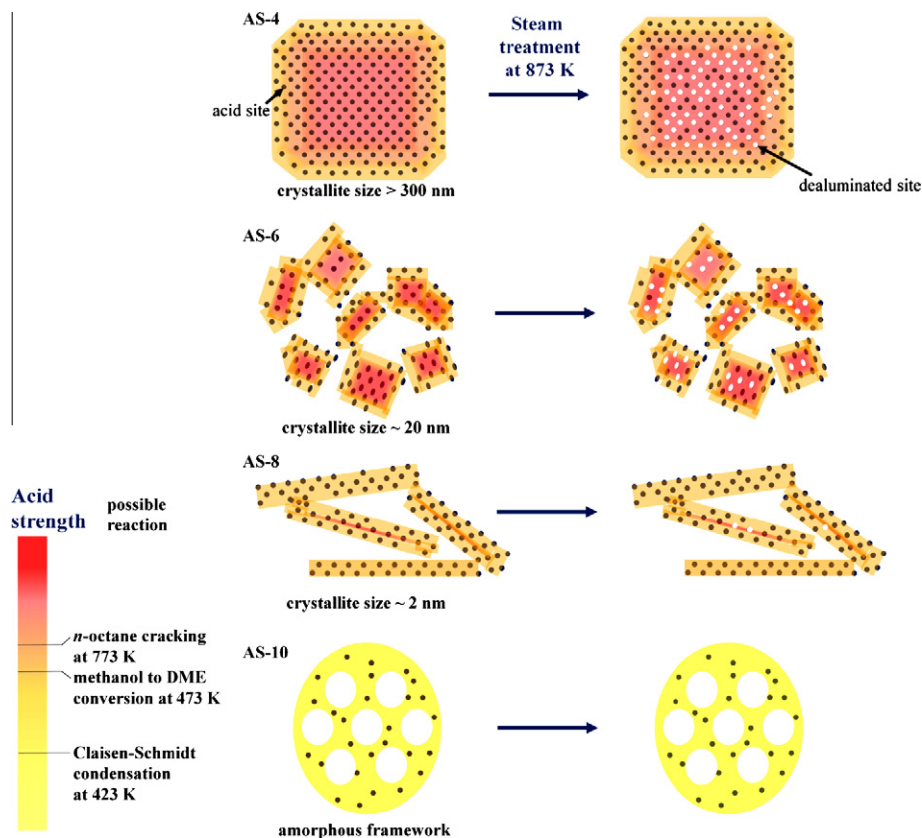
sites. The result confirms that external acid sites have relatively weaker acid strength than the internal sites. AS-10 samples showed the smallest fraction of strong acid sites among the materials due to amorphous framework. After the steam treatment, more significant loss of strong acid sites was observed for the zeolitic materials with a larger crystallite size. The AS-4 with a submicron crystallite size exhibited 33% loss, while AS-8 with 2–6 nm crystallites showed only 2% loss. By combining the results in Figs. 6 and 7, we can conclude that the external acid sites of zeolites possess somewhat weaker acid strength than the internal acid sites, but still stronger than acid sites in an amorphous framework. Furthermore, the external acid sites are remarkably more stable against steam dealumination than the internal acid sites (Scheme 2).

3.4. Catalytic properties of the aluminosilicate materials

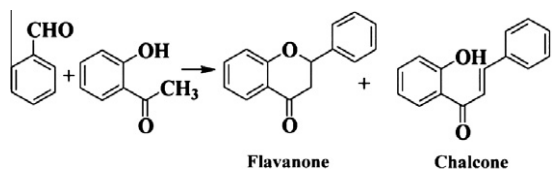
The catalytic consequences of pore structure, acid site distribution, strength, and hydrothermal stabilities of the aluminosilicate materials were systemically investigated by conversion of methanol to dimethylether (DME), MTG (methanol-to-gasoline) reaction, cracking of *n*-octane, and the flavanone synthesis that is the Claisen–Schmidt condensation (Scheme 3).

In methanol conversion to DME (Table 2), methanol with a small kinetic diameter (0.37 nm) [47] can freely diffuse into the 10-membered channel (0.51–0.56 nm) of MFI zeolite and all the acid sites are accessible. The catalytic measurement showed that the activities increased in the order AS-8 < AS-4 < AS-6 which corresponds to the order of increasing total acid concentration. Considering that the materials possess significantly different internal/external distribution of acid sites, such results indicate that both internal and external acid sites can similarly catalyze the DME synthesis reaction. It is noteworthy that the catalytic activities of the AS-8 and AS-4 samples were reversed after the steam treatment. This can be ascribed to the much higher resistance of the external acid sites against steam dealumination than the internal acid sites. The AS-10 sample showed negligible catalytic conversion at 473 K, indicating that the acid sites in the amorphous framework possess too weak acid strength to catalyze the methanol to DME conversion at 473 K. The similar catalytic results were also observed in the MTG reaction at 623 K (Table 2).

Catalytic measurements of the flavanone synthesis reaction (Table 1) showed that the catalytic activity of the zeolitic materials increased with a decreasing zeolite crystallite size (AS-4 < AS-6 < AS-8). The result is consistent with the previous report showing



Scheme 2. Schematic demonstration of the spatial distribution, strength, and steam stability of the acid sites in the aluminosilicate samples directed by gemini-surfactants.



Scheme 3. Claisen-Schmidt condensation for flavanone synthesis.

that the reaction is catalyzed only by the external acid sites due to the large molecular species involved in the reaction [29]. The AS-10 sample also showed some activities, indicating that the reaction can be catalyzed by relatively weak acid sites in the amorphous aluminosilicate framework. All the samples exhibited almost unchanged catalytic activities after steam treatment. The result can be attributed to the high hydrothermal stability of external acid sites, which is consistent with our IR study.

As seen in the cases of DME and the flavanone synthesis reaction, different acid-catalyzed reactions require different acid strengths. A variety of correlations of catalytic activity and sites of a certain acid strength range have been reported [48]. With this in mind, the question arises of whether the external acid sites in nanocrystalline zeolites could catalyze the reactions requiring the highest acid strength such as alkane cracking reaction. Our IR study showed that the external acid sites possess somewhat lower acid strength than the internal sites. To answer this question, we chose two samples, the AS-4 and ST-8 samples, for carrying out an *n*-octane cracking reaction. The AS-4 sample contained mainly the internal acid sites (97%), while ST-8 mainly contained the external sites (89%). AS-4 and ST-8 samples showed 15.5% and 8.5% conversion, respectively. Even if we consider the lower concentration of total acid sites in ST-8 (0.25 mmol g^{-1}) than AS-4 (0.34 mmol g^{-1}),

Table 2
Catalytic data for the aluminosilicate materials in methanol to DME conversion, MTG reaction, and flavanone synthesis.

Sample	Conversion (%)		
	Methanol to DME conversion ^a	MTG reaction ^b	Flavanone synthesis ^c
AS-4	38.0	24.7	3.0
ST-4	11.0	10.0	2.8
AS-6	47.2	29.6	27.2
ST-6	25.4	22.1	25.4
AS-8	24.1	17.3	30.2
ST-8	23.3	17.7	28.4
AS-10	≤1	≤1	21.6
ST-10	≤1	≤1	19.8

^a Reaction condition: methanol (WHSV = $9.5 \text{ g g}^{-1} \text{ h}^{-1}$) in N_2 flow (50 ml min^{-1} flow rate), catalyst 0.05 g, 473 K, measured at time-on-stream = 30 min.

^b Reaction condition: methanol (WHSV = $19 \text{ g g}^{-1} \text{ h}^{-1}$) in N_2 flow (50.5 ml min^{-1} flow rate), catalyst 0.05 g, 623 K, measured at time-on-stream = 30 min.

^c Reaction condition: benzaldehyde (7 mmol), 2-hydroxyacetophenone (3.5 mmol), catalyst 0.05 g, 423 K, reaction time 6 h.

the catalytic conversion per acid site was still 34% higher in AS-4 than ST-8 sample. Such results indicate that intrinsic activity of internal acid sites is higher than that of external acid sites. The high activity of internal acid sites might be ascribed to both of the intrinsically lower deprotonation enthalpies or stronger heat of adsorption than external acid sites. Gounder et al. reported that both of the deprotonation enthalpies and stabilization of reactants and cationic transition state in the confined spaces ('solvation effect') affects the catalytic activity in alkane activation [49]. More detailed studies combining reaction kinetics and thermochemical studies would be required to clarify the contributions of these two parameters. Nevertheless, our results clearly reveals that the

external acidity can still catalyze the alkane cracking reaction, while showing remarkably enhanced hydrothermal stability.

4. Conclusions

In summary, nanocrystalline MFI zeolites having different crystallite shapes and sizes (2–300 nm) were hydrothermally synthesized using gemini-surfactants. FT-IR spectroscopy using pyridine and 2,6-di-tert-butylpyridine as a base probe revealed that the amount of external acid sites increased with a decreasing crystallite size. The external sites were weaker than the internal sites in acid strength, but they could still catalyze the reactions requiring very strong acidity such as alkane cracking and MTG reaction. Most notably, the external acid sites showed remarkably higher stability against steam dealumination than the internal sites. To the best of our knowledge, such extraordinary steam stability of external acid sites has not been reported so far, probably due to the negligible concentration of these sites in conventional zeolites. Although the present conclusion was demonstrated for MFI zeolites synthesized using gemini-surfactants, we believe that the observations can be generalized to other zeolite materials. It is expected that the nanocrystalline zeolites having abundant external acid sites would provide the significant benefits of high hydrothermal stability of acid sites and hence catalytic reusability, in addition to the well-known advantages of enhanced mass transfer and high catalytic activities for large molecules. Nanocrystalline zeolites, however, would not be advantageous for reactions requiring high shape selectivity (e.g., *p*-xylene synthesis) due to the large amount of external acid sites that can catalyze the reaction non-selectively [50].

Acknowledgments

This work was supported by the General Project of the Korea Institute of Geoscience and Mineral Resources (KIGAM) funded by the Ministry of Knowledge Economy of Korea and also by Basic Science Research Program through the National Research Foundation of Korea (NRF) funded by the Ministry of Education, Science and Technology (20110011392).

Appendix A. Supplementary material

Supplementary data associated with this article can be found, in the online version, at [doi:10.1016/j.jcat.2012.01.009](https://doi.org/10.1016/j.jcat.2012.01.009).

References

- [1] C.S. Cundy, P.A. Cox, *Chem. Rev.* 103 (2003) 663.
- [2] T.F. Degnan Jr., *Top. Catal.* 13 (2000) 349.
- [3] A. Corma, *Chem. Rev.* 97 (1997) 2373.
- [4] A. Corma, *J. Catal.* 216 (2003) 298.
- [5] K. Egeblad, C.H. Christensen, M. Kustova, C.H. Christensen, *Chem. Mater.* 20 (2008) 946.
- [6] Y. Tao, H. Kanoh, L. Abrams, K. Kaneko, *Chem. Rev.* 106 (2006) 896.
- [7] J. Pérez-Ramírez, C.H. Christensen, K. Egeblad, C.H. Christensen, J.C. Groen, *Chem. Soc. Rev.* 37 (2008) 2530.
- [8] A. Corma, M.J. Díaz-Cabañas, J.L. Jordá, C. Martínez, M. Moliner, *Nature* 443 (2006) 842.
- [9] M.E. Davis, C. Saldarriaga, C. Montes, J. Garces, C. Crowder, *Nature* 331 (1988) 698.
- [10] M.E. Davis, *Nature* 417 (2002) 813.
- [11] C.T. Kresge, M.E. Leonowicz, W.J. Roth, J.C. Vartuli, J.S. Beck, *Nature* 359 (1992) 710.
- [12] D.Y. Zhao, J.L. Feng, Q.S. Huo, N. Melosh, G.H. Fredrickson, B.F. Chmelka, G.D. Stucky, *Science* 279 (1998) 548.
- [13] J.Y. Ying, C.P. Mehnert, M.S. Wong, *Angew. Chem. Int. Ed.* 38 (1999) 56.
- [14] K. Cassiers, T. Linssen, M. Mathieu, M. Benjelloun, K. Schrijnemakers, P. van der Voort, P. Cool, E.F. Vansant, *Chem. Mater.* 14 (2002) 2317.
- [15] L. Tosheva, V.P. Valtchev, *Chem. Mater.* 17 (2005) 2494.
- [16] J.C. Groen, J.C. Jansen, J.A. Moulijn, J. Pérez-Ramírez, *J. Phys. Chem. B* 108 (2004) 13062.
- [17] S. van Donk, A.H. Janssen, J.H. Bitter, K.P. de Jong, *Catal. Rev. Sci. Eng.* 45 (2003) 297.
- [18] C.J.H. Jacobsen, C. Madsen, J. Houzvicka, I. Schmidt, A. Carlsson, *J. Am. Chem. Soc.* 122 (2000) 7116.
- [19] M. Choi, K. Na, J. Kim, R. Srivastava, C. Venkatesan, D.H. Choi, R. Ryoo, *Nat. Mater.* 5 (2006) 718.
- [20] H. Wang, T.J. Pinnavaia, *Angew. Chem. Int. Edit.* 18 (2006) 2462.
- [21] M. Choi, K. Na, J. Kim, Y. Sakamoto, O. Terasaki, R. Ryoo, *Nature* 461 (2009) 246.
- [22] K. Na, C. Jo, J. Kim, K. Cho, J. Jung, Y. Seo, R.J. Messinger, B.F. Chmelka, R. Ryoo, *Science* 333 (2011) 328.
- [23] J.C. Groen, W. Zhu, S. Brouwer, S.J. Huynink, F. Kapteijin, J.A. Moulijn, J. Pérez-Ramírez, *J. Am. Chem. Soc.* 129 (2007) 355.
- [24] C.H. Christensen, K. Johannsen, E. Törnqvist, I. Schmidt, H. Topsøe, C.H. Christensen, *Catal. Today* 128 (2007) 117.
- [25] K. Cho, R. Ryoo, S. Asahina, C. Xiao, M. Klingstedt, A. Umemura, M.W. Anderson, O. Terasaki, *Solid State Sci.* 13 (2011) 750.
- [26] C.H. Christensen, K. Johannsen, I. Schmidt, C.H. Christensen, *J. Am. Chem. Soc.* 125 (2003) 13370.
- [27] D.L. Moushey, P.G. Smirniotis, *Catal. Lett.* 129 (2009) 20.
- [28] P.-H. Chao, S.-T. Tsai, S.-L. Chang, I. Wang, T.-C. Tsai, *Top. Catal.* 53 (2010) 231.
- [29] V.N. Shetti, J. Kim, R. Srivastava, M. Choi, R. Ryoo, *J. Catal.* 245 (2008) 296.
- [30] J. Kim, M. Choi, R. Ryoo, *J. Catal.* 269 (2010) 219.
- [31] R. Srivastava, M. Choi, R. Ryoo, *Chem. Commun.* (2006) 4489.
- [32] K. Suzuki, Y. Aoyagi, N. Katada, M. Choi, R. Ryoo, M. Niwa, *Catal. Today* 132 (2008) 38.
- [33] D. Verboekend, L.A. Villaescusa, K. Thomas, I. Stan, J. Pérez-Ramírez, *Catal. Today* 152 (2010) 11.
- [34] C. Fernandez, I. Stan, J.-P. Gilson, K. Thomas, A. Vicente, A. Bonilla, J. Pérez-Ramírez, *J. Chem. Eur. J.* 16 (2010) 6224.
- [35] Y. Li, D. Liu, W. Wang, S. Xie, X. Zhu, L.J. Xu, *Nat. Gas Chem.* 17 (2008) 69.
- [36] D.W. Fickel, R.F. Lobo, *J. Phys. Chem. C* 114 (2010) 1633.
- [37] D.W. Fickel, E. D'Addio, J.A. Lauterbach, R.F. Lobo, *Appl. Catal. B: Environ.* 102 (2011) 441.
- [38] A. Corma, V. Fornés, L. Forni, F. Márquez, J. Martínez-Triguero, D. Moscotti, *J. Catal.* 179 (1998) 451.
- [39] L.W. Beck, M.E. Davis, *Microporous Mesoporous Mater.* 22 (1998) 107.
- [40] R. Ryoo, J.M. Kim, C.H. Ko, C.H. Shin, *J. Phys. Chem.* 100 (1996) 17718.
- [41] J.S. Beck, J.C. Vartuli, G.J. Kennedy, C.T. Kresge, W.J. Roth, S.E. Schramm, *Chem. Mater.* 6 (1994) 1816.
- [42] B.J. Schoeman, *Microporous Mesoporous Mater.* 22 (1998) 9.
- [43] K.S.W. Sing, *Pure Appl. Chem.* 57 (1985) 603.
- [44] M. Kruk, M. Jaroniec, Y. Sakamoto, O. Terasaki, R. Ryoo, C.H. Ko, *J. Phys. Chem. B* 104 (2000) 292.
- [45] E.R. Parry, *J. Catal.* 2 (1963) 371.
- [46] J. Dewing, G.T. Monks, B. Youll, *J. Catal.* 44 (1976) 226.
- [47] M. Choi, Z. Wu, E. Iglesia, *J. Am. Chem. Soc.* 132 (2010) 9129.
- [48] C.N. Satterfield, *Heterogeneous Catalysis in Industrial Practice*, second ed., Krieger publishing company, Malabar, Florida, 1996.
- [49] R. Gounder, E. Iglesia, *J. Am. Chem. Soc.* 131 (2009) 1958.
- [50] Z.L. Hua, J. Zhou, J.L. Shi, *Chem. Commun.* 47 (2011) 10536.